25-29 August 2024
inter.noise
NANTES FRANCE

Experimental characterization of stall noise on a pitching airfoil in an anechoic wind tunnel

Benjamin Cotté[1], Lisa Sicard, David Raus, Romain Monchaux
IMSIA, ENSTA Paris, Institut Polytechnique de Paris
91120 Palaiseau, France

Emmanuel Jondeau, Pascal Souchotte, Michel Roger
LMFA, École Centrale de Lyon, Université de Lyon
69131 Écully, France

ABSTRACT

Dynamic stall noise is one of the potential source of amplitude modulations associated with wind turbine noise. This phenomenon is related to the periodic separation and reattachment of the boundary layer on the wind turbine blade suction side during its rotation. Within the framework of the PIBE project (Predicting the Impact of Wind Turbine Noise), experiments were conducted in an anechoic wind tunnel in order to characterize stall noise on a pitching airfoil in both static and dynamic conditions. A first set of measurements was performed using an airfoil equiped with pressure taps to measure both steady and unsteady wall pressure as well as far-field acoustic pressure. These measurements were used to identify the noise regimes associated with different angles of attack, and to relate them with the boundary layer evolution. In a second experiment, synchronized flow and acoustic measurements have been obtained to identify the coherent aerodynamic structures responsible for the noise radiation. The velocity fluctuations evaluated from the time-resolved particle image velocimetry (TR-PIV) data are correlated with acoustic pressure to localize aeroacoustic sources, and various tools such as vortex detection methods and spectral proper orthogonal decomposition are applied to identify the nature of these sources.

1. INTRODUCTION

As explained by Oerlemans [1], local stall can occur on wind turbine blades during the upper part of the revolution in presence of a strong wind shear, or another source of inhomogeneous inflow such as yaw or topography. As a result, periodic separation and reattachment of the boundary layer can occur on the wind turbine blade suction side during its rotation. As stall noise is associated with a strong low-frequency increase [2, 3], this could explain the strong amplitude modulations of wind turbine noise that are commonly observed around wind farms.

One of the objectives of the PIBE project (Predicting the Impact of Wind Turbine Noise) is to characterize dynamic stall noise in controlled conditions, in order to improve its modeling and develop techniques to mitigate it in the context of wind turbines. For a static airfoil, a few studies have been conducted to characterize separation/stall noise, see e.g. Refs. [2–4], and the mechanisms at the origin of the noise are more or less understood. For a pitching airfoil, on the

[1]benjamin.cotte@ensta-paris.fr

other hand, the number of studies are limited [5, 6], and the turbulent structures at the origin of the noise are not clearly identified. In particular, the aerodynamic properties are known to vary significantly depending on the pitching frequency, with the presence of a dynamic stall vortex only above a given reduced frequency [7].

During a first campaign, experiments were conducted in an anechoic wind tunnel on a NACA 0012 airfoil equiped with pressure taps. Some results of this campaign were analyzed in Ref. [8], and will not be detailed here. During a second experimental campaign, we investigated the noise radiation of a NACA$63_3$418 airfoil, that is typically used on the outer part of wind turbine blades. In this paper, an overview of the aerodynamic and acoustic measurements performed on this airfoil is presented, both in the static and dynamic regimes. Due to the limited size of this conference proceeding, we present only results for the NACA63(3)418 airfoil equiped with pressure taps. Experimental results obtained with synchronous acoustic and flow mesurements can be found in Ref. [9].

2. EXPERIMENTAL SETUP

The experiments were performed in the anechoic wind tunnel of the Ecole Centrale de Lyon. This wind tunnel consists of an open jet with a rectangular 0.4 m × 0.3 m nozzle exit, enclosed in an anechoic chamber of dimensions 8 m × 9 m × 10 m, with a cut-off frequency below 100 Hz. Two horizontal end-plates are installed downstream of the nozzle exit in order to guide the incoming flow. Two airfoils of chord c = 12 cm and of span s = 30 cm were tested: a NACA0012 airfoil and a NACA$63_3$418 airfoil, as shown in Figure 1. The pitching motions of the airfoil are driven by a motor placed beneath the lower end-plate. The airfoil is centered on the discs so that it rotates about its center-chord.

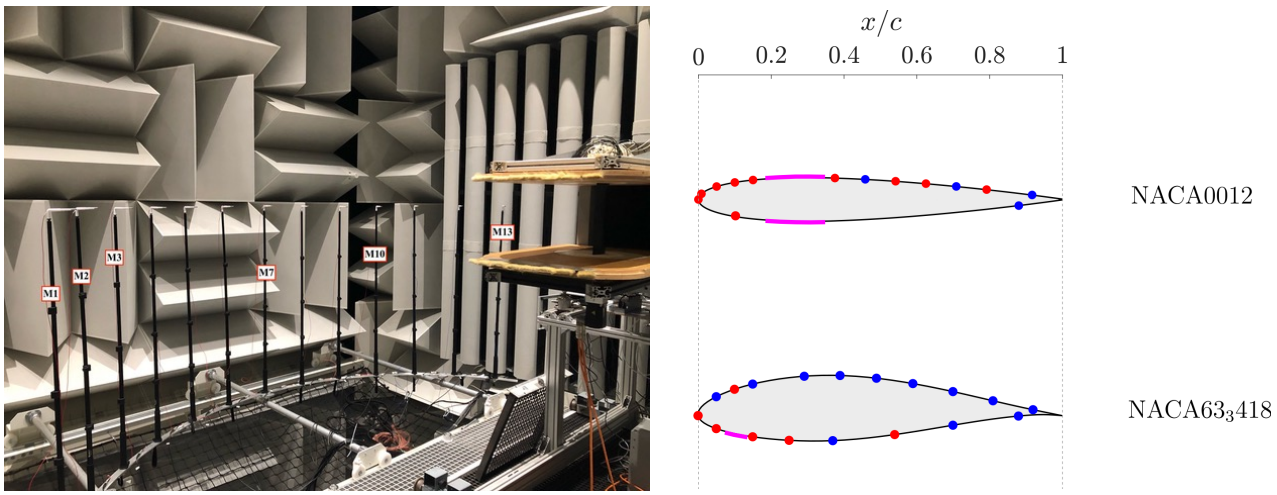

(a) (b)

Figure 1: (a) View of the experimental setup with nozzle exit, the airfoil placed vertically between the end-plates and the array of 13 microphones, and (b) positions of the pressure taps on the airfoils. Red dots and blue dots show the positions where only the steady-state surface pressure is measured and the positions where both the steady and fluctuating wall pressures are measured, respectively. Purple areas show the positions of the tripping tape.

The airfoils were subjected to a flow of free-stream velocity U equal to 25 m/s, 50 m/s and 75 m/s, corresponding to chord-based Reynolds numbers of approximately 2×10^5, 4×10^5 and 6×10^5. In order to force transition to turbulent boundary layers on the airfoil and to avoid the generation of the laminar boundary layer tonal noise at low incidence, we use either a turbulence grid or a tripping device. In the case called hereafter with grid, the tripping device is not used, and an homogeneous and isotropic turbulence is generated with an integral length scale Λ = 8 mm,

and a turbulence intensity $TI = u'_{\text{rms}}/U = 1.6\%$, with u'_{rms} the root mean square value of the velocity fluctuations. In the case called hereafter with tripping, the incoming flow is characterized by a low turbulence intensity, with $u'_{\text{rms}}/U = 0.4\%$, and the airfoil is tripped on the pressure side between $x/c = 0.1$ and $x/c = 0.15$.

In a given static configuration, measurements are performed at geometric angles of attack noted α_g. In dynamic configurations, the airfoils are subjected to a sinusoidal pitching motion about their center chord:

$$\alpha_g = \alpha_0 + \alpha_1 \sin(2\pi f_0 t), \tag{1}$$

where f_0 is the oscillation frequency, α_0 is the mean angle of attack and α_1 is the amplitude of the angle of attack variation. These angles are the geometric angles of attack fixed by the motor. In an open-jet wind tunnel, the flow deviates from the nozzle axis because of the presence of the airfoil. The effective angles of attack of the airfoil is thus smaller than the geometric values. Incidence corrections can be applied, as shown in [8], but they have not been validated for an oscillating airfoil. In the following, only geometric angles of attack are used.

In this paper, only results from the experimental campaign with the NACA$63_3$418 airfoil will be presented. For a static airfoil, both the cases with grid and with tripping will be considered, at the three incoming velocities. For an oscillating airfoil, only the case with tripping will be shown for an angle of attack of $15° \pm 15°$, for the flow velocities U and oscillating frequencies f_0 given in Table 1. The reduced frequency is defined as $k = \pi f_0 c/U$, and varies between 0.005 and 0.05 depending on the experimental parameters. The boundary between quasi-steady and dynamic stall can be estimated using the reduced pitch rate defined as $k_\star = \alpha_1 k$. Sheng *et al.* [10] found a threshold of $k_\star = 0.01$ for NACA airfoils. In the present paper, we expect all the regimes to be quasi-steady, except at 25 m/s for a reduced frequency $k = 0.05$.

Table 1: Parameters associated with the six oscillating airfoil configurations.

U (m/s)	α_0 (°)	α_1 (°)	f_o (Hz)	k	$k^\star$
25	15	15	0.66	0.01	2.6×10^{-3}
25	15	15	1.66	0.025	6.5×10^{-3}
25	15	15	3.32	0.05	1.3×10^{-2}
50	15	15	0.66	0.005	1.3×10^{-3}
50	15	15	1.33	0.01	2.6×10^{-3}
50	15	15	3.32	0.025	6.5×10^{-3}

The two airfoils are instrumented with pinholes located mid-span, along the chord of the airfoils. These pin-holes are connected by capillary tubes to a Kulite KMPS-1-64 pressure scanner to measure the steady wall pressure at a sampling frequency $f_s = 1.1$ kHz. As shown in Fig. 1b, few of the pin-holes are also connected to Brüel & Kjær 4958 type microphones through a T-junction to acquire the fluctuating wall pressure signals at a sampling frequency $f_s = 51.2$ kHz. This Remote-Microphone Probe (RMP) technology and the in-situ calibration of the microphones are described in Reference [11]. The positions of the surface pressure measuring points are shown in Fig. 1b. Far-field noise measurements were performed with Gras 46BE microphones at a sampling frequency $f_s = 51.2$ kHz. For the campaign with the NACA$63_3$418 airfoil, set of 13 microphones placed in the mid-span, 2 meters away from the airfoil center-chord, as shown in Figure 1(b). The microphones are facing the airfoil pressure side. The angles θ with respect to the inflow velocity stream are given in Table 2, $\theta = 0°$ corresponding to the downstream direction. In order to characterize the background noise generated by the wind tunnel and the end plates, far-field noise measurements

are also performed in the same wind conditions but without the airfoil in the test section. The sources of the background noise (noise of the jet, trailing-edge noise of the horizontal plates...) are assumed to be identical when the airfoil is added in the test section. Precautions must be taken at very high angles of attack, as the background noise could be slightly modified at low frequencies because of the airfoil [2]. Note that flow measurements using time-resolved particle image velocimetry have also been performed with another NACA63$_3$418 airfoil without pressure taps. Some results are presented in Ref. [9].

Table 2: Angle θ of the far-field microphones with respect to the inflow velocity stream.

Numéro	**1**	**2**	**3**	**4**	**5**	**6**	**7**	**8**	**9**	**10**	**11**	**12**	**13**
θ (°)	30	40	50	60	70	80	90	100	110	120	130	140	150
Oscillating airfoil													

3. RESULTS

3.1. Static airfoil

We consider first the evolution of the lift coefficient with respect to the angle of attack α_g, plotted in Figure 2 in the cases with tripping and with grid for the three incoming velocities. The curves are almost identical up to approximately 14°, close to the static stall angle. In the case with tripping, the maximum lift coefficient varies slightly with respect to Reynolds number, and the lift sudden drop associated with the complete detachment of the boundary layer occurs at different angles of attack between 22 and 25°. In the case with grid, on the other hand, the three curves overlap almost perfectly.

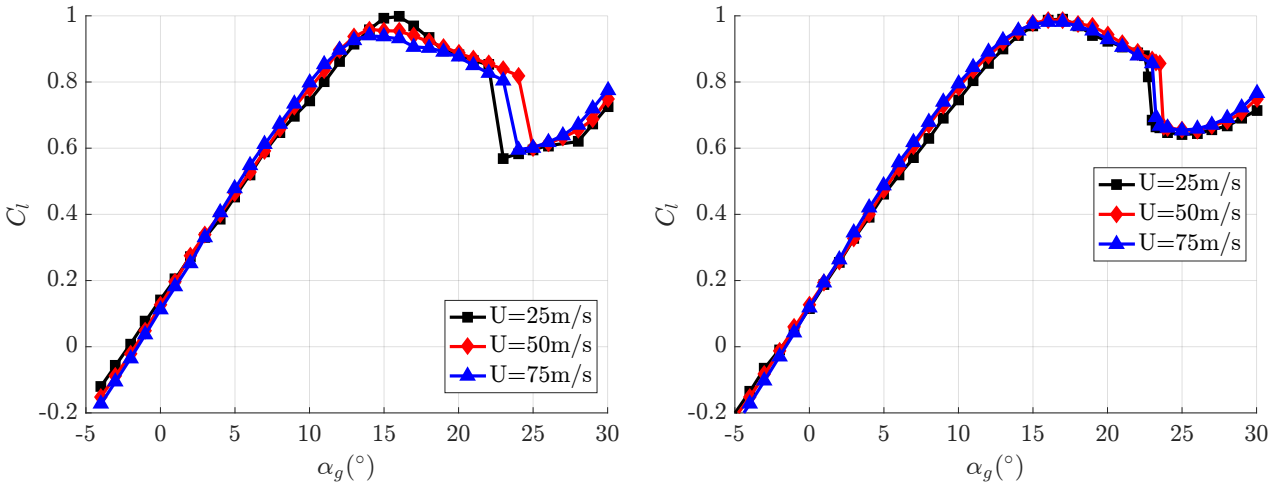

(a) (b)

Figure 2: Lift coefficient in the cases (a) with tripping and (b) with grid.

The power spectral density (PSD) of acoustic pressure at microphone 7 ($\theta = 90°$) is plotted in Figure 3 for various incidence angles at $U = 50$ m/s. In the case with tripping, the spectrum at $\alpha_g = 2°$ is close to the background noise, with a significant signal to noise ratio between 800 Hz and 1800 Hz approximately. At these low angles of attack, the main noise mechanism is associated with the interaction between turbulent boundary layer fluctuations and the airfoil trailing edge. At

$\alpha_g = 18°$, the boundary layer is partially separated, and the noise spectrum increases significantly between 200 Hz and 1000 Hz; this corresponds to separation noise. Then at $\alpha_g = 25°$, where the boundary layer is completely separated, the noise radiation is significantly above the background noise for all frequencies between 70 Hz and 10 kHz. This is sometimes called the light stall regime in the literature. Finally, at the maximum incidence angle of 30°, a strong narrowband peak appears around 160 Hz, which corresponds to a projected Strouhal number $Uc \sin \alpha_g / U \approx 0.19$. At this angle of attack, the airfoil behaves like a bluff body, which corresponds to the deep stall noise regime. In the case with grid, there is a significant increase in noise radiation between 200 Hz and 3 kHz. This can be attributed to turbulence interaction noise.

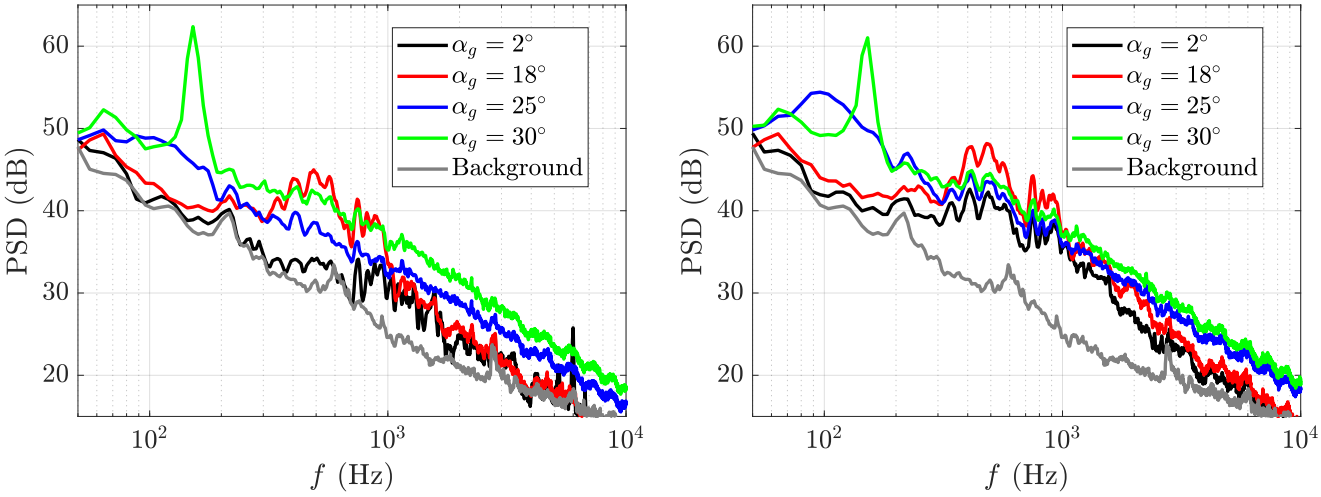

Figure 3: Power spectral densities of acoustic pressure in the cases (a) with tripping and (b) with grid.

In order to evaluate the sensitivity of the acoustic spectrum to Reynolds number, the PSD are plotted for three incoming velocities and the same four angles of attack in Figure 4. Note that the background noise is not plotted in this figure. As seen in Figure 3 for $U = 50$ m/s, the signal to noise ratio is quite low at $\alpha_g = 2°$ for the other flow velocities, and increases for larger incidence angles. The difference between the cases with and without turbulence grid is maximal for $\alpha_g = 2°$, with an increase of up to 8 dB that is associated to turbulence interaction noise. At an incidence angle of 30°, a tonal peak is consistently found for a Strouhal number of 0.36, corresponding to a projected Strouhal number $Uc \sin \alpha_g / U \approx 0.19$. The influence of the turbulence grid is small in this deep stall noise regime.

The PSD for all the microphones of the array are plotted in Figure 5 for in the case with grid. For both $\alpha_g = 25°$ and $\alpha_g = 30°$, there is a stronger noise radiation upstream, for radiation angles around 120°. In the deep stall noise regime, for $\alpha_g = 30°$, the tonal peak at $St \approx 0.36$ is present in all radiation angles, and its amplitude increases when θ increases. A second peak at $St \approx 0.72$ appears for radiations angles above 120°.

4. OSCILLATING AIRFOIL

We focus here on the results for $U = 25$ m/s and 50 m/s in the case with tripping, for the reduced frequencies given in Table1. First, the evolution of the phase-averaged lift coefficient with the angle of attack is plotted in Figure 6 for all the reduced frequencies. The curve in the static regime is also shown as a reference. The curves for the oscillating airfoil follow the static airfoil curve up to the static stall angle around 15°. Then, a lift overshoot is observed, that increases with the reduced frequency k, as classically observed in the literature; see Ref. [8] and references

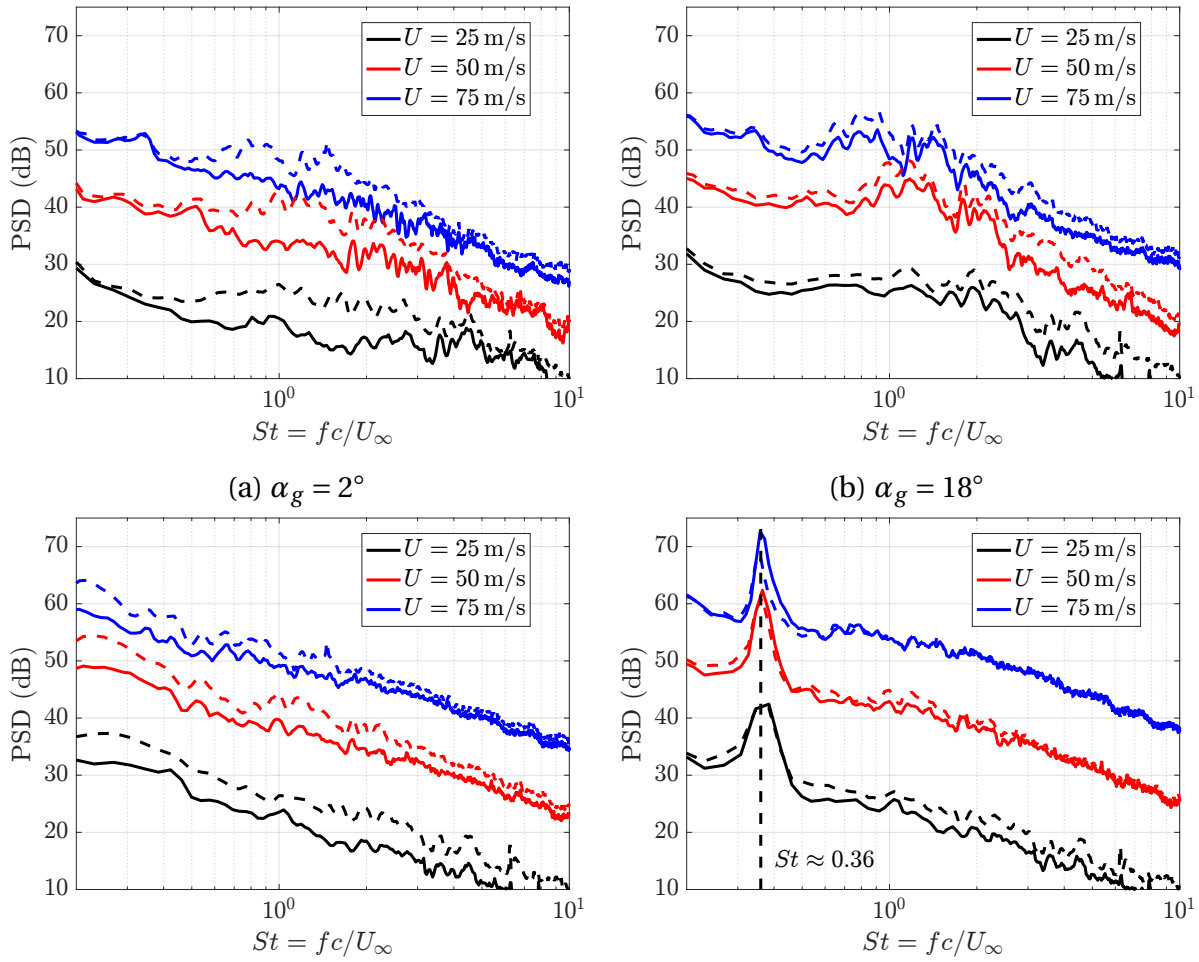

(a) $\alpha_g = 2°$ (b) $\alpha_g = 18°$

(c) $\alpha_g = 25°$ (d) $\alpha_g = 30°$

Figure 4: Power spectral densities of acoustic pressure for different angles of attack. The solid lines correspond to the case with tripping, and the dashed lines correspond to the case with grid.

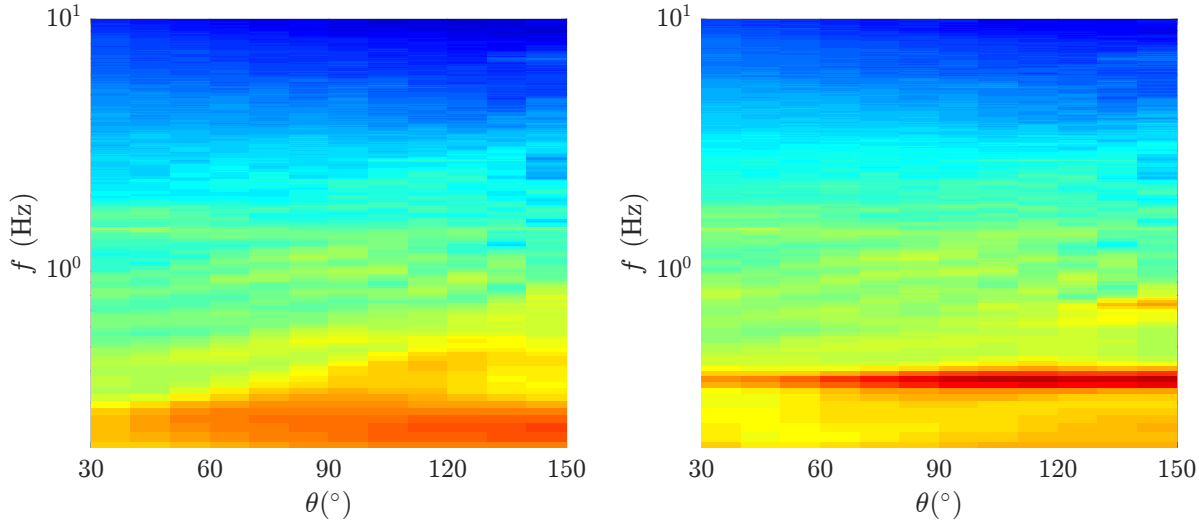

(a) $\alpha_g = 25°$ (b) $\alpha_g = 30°$

Figure 5: Power spectral densities of acoustic pressure for all 13 radiation angles with respect to microphone angle for two angles of attack in the case with grid. The color bar is between 20 and 65 dB

therein. When the angle of attack decreases from 30° the lift coefficient drops to values close to the static ones. The higher the reduced frequency, the later the boundary layer reattaches. Overall, the hysteresis loop strongly increases when k increases from 0.01 to 0.05 for $U = 25\,\mathrm{m/s}$, and from 0.005 to 0.025 for $U = 50\,\mathrm{m/s}$. Even though the reduced frequencies of 0.005 and 0.01 correspond to the quasi-static regime according to the literature, a significant increase of the hysteresis loop is seen between these two oscillation frequencies.

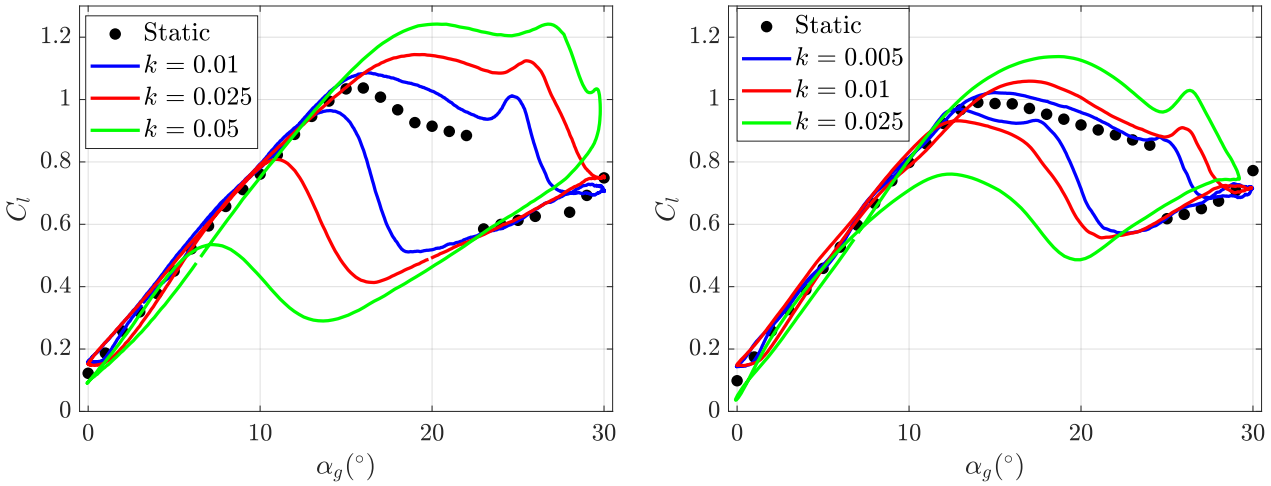

(a) $U = 25\,\mathrm{m/s}$ (b) $U = 50\,\mathrm{m/s}$

Figure 6: Phased-averaged lift coefficient for the oscillating airfoil at different reduced frequencies k.

To better assess the effect of the Reynolds number on the evolution of the lift coefficient, the curves are compared in Figure 7 for reduced frequencies of 0.01 and 0.025. The curves are quite similar, although the lift coefficient reaches slightly higher values at large increasing angles of attack for $U = 25\,\mathrm{m/s}$. Also, the boundary layer tends to reattach at lower decreasing angles of attack for $U = 25\,\mathrm{m/s}$.

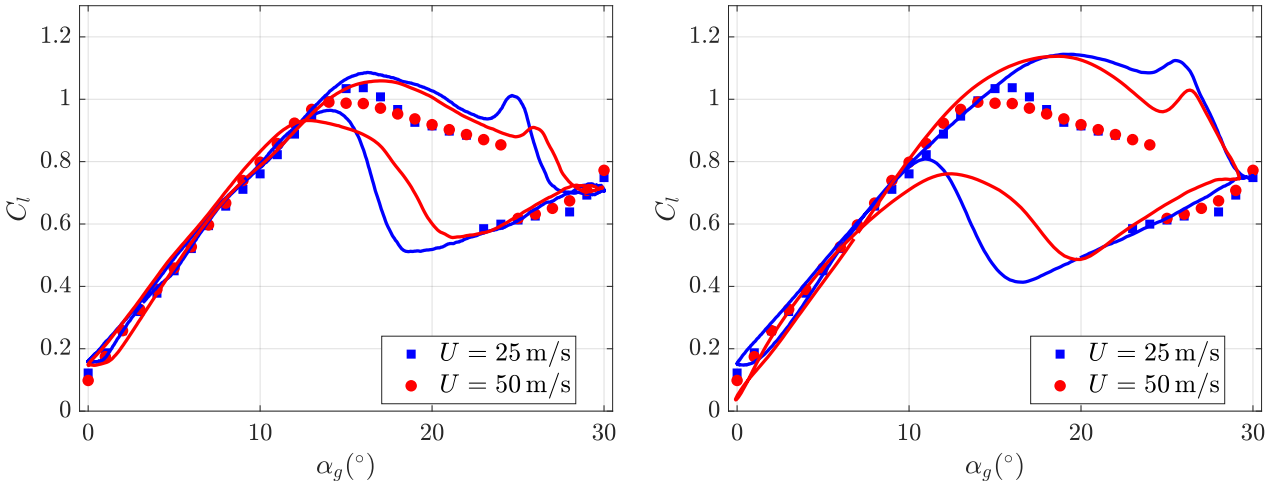

(a) $k = 0.01$ (b) $k = 0.25$

Figure 7: Comparison of the phased-averaged lift coefficient for $U = 25\,\mathrm{m/s}$ and $U = 50\,\mathrm{m/s}$ for the oscillating airfoil (solid lines). The symbols correspond to the data for the static airfoil.

Phased-averaged spectrograms of acoustic pressure are calculated with a frequency resolution of 6 Hz and an overlap of 80%. The temporal resolution correspond to $t_c/50$, where

$t_c = 1/f_0$ is the oscillation period. The spectrograms are plotted in Figure 8 for all cases except the reduced frequency $k = 0.05$ for $U = 25\,\mathrm{m/s}$, because this measurement is contaminated by motor noise. For the quasi-static regimes at $k = 0.005$ and $k = 0.01$, a strong broadband noise increase is visible at $f_0 t = 0.4$, corresponding to the complete boundary layer separation (light stall noise). Then, a narrowband peak around a Strouhal number of 0.36 is present up to $f_0 t = 0.7$ (deep stall noise), followed by a broadband noise associated with the boundary layer reattachment. For the reduced frequency $k = 0.025$, which is an intermediate case between the quasi-static and the dynamic regimes, a similar shape is observed but with stronger levels, especially during the boundary layer separation around $f_0 t = 0.4$.

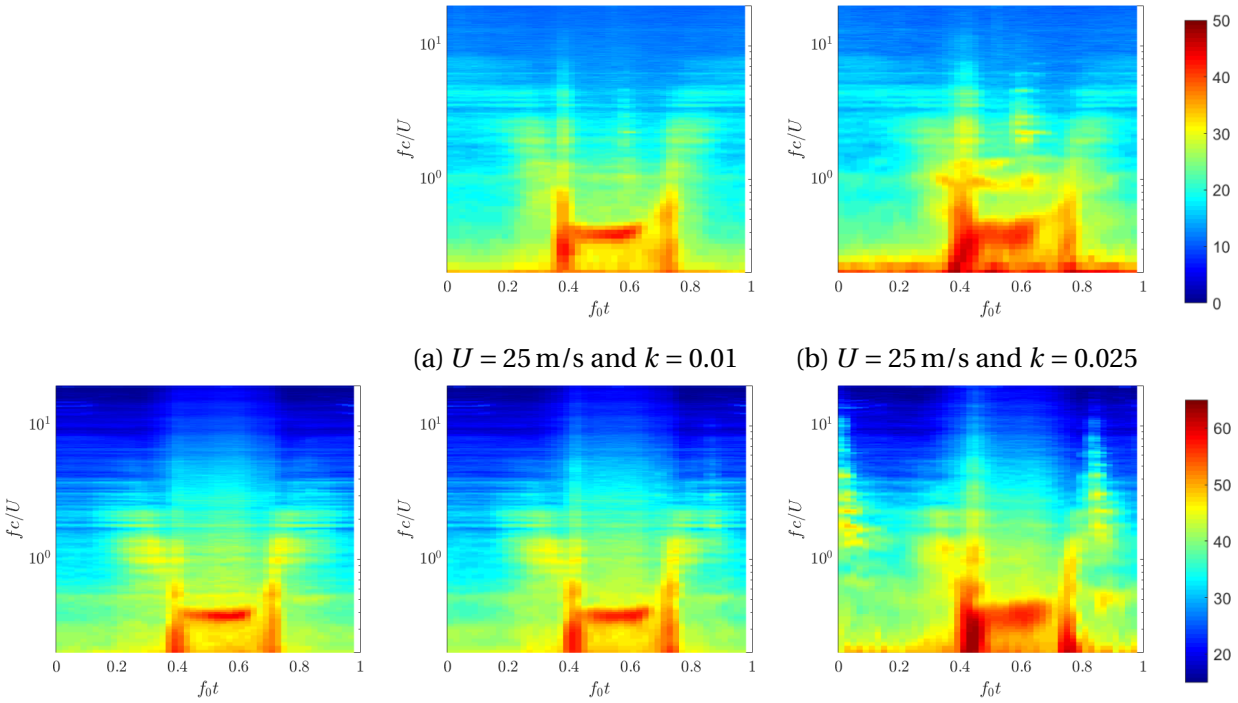

(a) $U = 25\,\mathrm{m/s}$ and $k = 0.01$ (b) $U = 25\,\mathrm{m/s}$ and $k = 0.025$

(c) $U = 50\,\mathrm{m/s}$ and $k = 0.005$ (d) $U = 50\,\mathrm{m/s}$ and $k = 0.01$ (e) $U = 50\,\mathrm{m/s}$ and $k = 0.025$

Figure 8: Phased-averaged spectrograms of acoustic pressure for different reduced frequencies k and different reduced frequencies U.

5. CONCLUSIONS

Within the framework of the PIBE project (Predicting the Impact of Wind Turbine Noise), an important experimental database has been collected in order to characterize airfoil stall noise both in static and dynamic regimes. Experiments have been performed with two different instrumented airfoil profiles, with different turbulence intensities and different chord-based Reynolds numbers. In addition, synchronized flow and acoustic measurements have been obtained to identify the coherent aerodynamic structures responsible for the noise radiation. This database will be made available to the scientific community to enable stall noise to be better understood, modeled and mitigated in the future.

ACKNOWLEDGEMENTS

This research is funded by the French National Agency for Research under grant agreement N°ANR-18-CE04-0011.

REFERENCES

1. Stefan Oerlemans. Effect of Wind Shear on Amplitude Modulation of Wind Turbine Noise. *International Journal of Aeroacoustics*, 14(5-6):715–728, October 2015.
2. Stephane Moreau, Michel Roger, and Julien Christophe. Flow Features and Self-Noise of Airfoils Near Stall or in Stall. In *15th AIAA/CEAS Aeroacoustics Conference (30th AIAA Aeroacoustics Conference)*, Miami, Florida, May 2009. American Institute of Aeronautics and Astronautics.
3. Franck Bertagnolio, Helge Aa. Madsen, Andreas Fischer, and Christian Bak. A semi-empirical airfoil stall noise model based on surface pressure measurements. *Journal of Sound and Vibration*, 387:127–162, January 2017.
4. Giovanni Lacagnina, Paruchuri Chaitanya, Tim Berk, Jung-Hoon Kim, Phillip Joseph, Bharathram Ganapathisubramani, Seyed Mohammad Hasheminejad, Tze Pei Chong, Oksana Stalnov, Kwing-So Choi, Muhammad Farrukh Shahab, Mohammad Omidyeganeh, and Alfredo Pinelli. Mechanisms of airfoil noise near stall conditions. *Physical Review Fluids*, 4(12):123902, December 2019.
5. Lars Siegel, Klaus Ehrenfried, Claus Wagner, Karen Mulleners, and Arne Henning. Cross-correlation analysis of synchronized piv and microphone measurements of an oscillating airfoil. *Journal of Visualization*, 21:381–395, 2018.
6. Y. Mayer, B. Zang, and M. Azarpeyvand. Aeroacoustic investigation of an oscillating airfoil in the pre- and post-stall regime. *Aerospace Science and Technology*, 103(105880), 2020.
7. K. Mulleners and M. Raffel. Dynamic stall development. *Exp. Fluids*, 54:1469, 2013.
8. David Raus, Benjamin Cotté, Romain Monchaux, Emmanuel Jondeau, Pascal Souchotte, and Michel Roger. Experimental study of the dynamic stall noise on an oscillating airfoil. *Journal of Sound and Vibration*, 537:117144, 2022.
9. L. Sicard, B. Cotté, and R. Monchaux. Experimental identification of airfoil stall noise sources in static and dynamic conditions. In *30th AIAA/CEAS Aeroacoustics Conference*, 2024.
10. W. Sheng, R. A. McD. Galbraith, and F. N. Coton. Prediction of Dynamic Stall Onset for Oscillatory Low-Speed Airfoils. *Journal of Fluids Engineering*, 130(10), 2008.
11. Michel Roger. Microphone measurements in aeroacoustic installations. *Design and Operation of Aeroacoustic Wind Tunnel Tests for Ground and Air Transport STO-AVT-287. Von Karman Institute for Fluid Dynamics*, 2017.